

# WAVE-PROPAGATION SIMULATION IN AN ELASTIC ANISOTROPIC (TRANSVERSELY ISOTROPIC) SOLID

By J. M. CARCIONE,† D. KOSLOFF

*(Department of Geophysics and Planetary Sciences, Tel Aviv University, Tel Aviv, Israel 69978)*

and R. KOSLOFF

*(Department of Physical Chemistry and The Fritz Haber Research Center for Molecular Dynamics, The Hebrew University, Jerusalem 91904, Israel)*

[Received 18 May 1987. Revise 18 September 1987]

## SUMMARY

A new formulation for wave-propagation simulation in a transversely isotropic material is presented. A pseudospectral time-integration technique to solve the equation of motion is used, where the propagation is done by a direct expansion of the evolution operator by a Chebycheff polynomial series. Examples of wave propagation in different homogeneous materials and comparison with analytical solutions in the symmetry axis, show that the new method is highly accurate. The present numerical simulation can be very important in determining the solution of elastodynamic problems when the analytical solutions are either very complicated or unknown.

## 1. Introduction

THE problem of wave propagation through anisotropic solids has been extensively studied by many researchers (see, for example, Musgrave (1) and Payton (2)), but exact analytical solutions of the wave field are very difficult to obtain, even in the most simple cases. The equations of motion for solids of low symmetry are extremely complicated. The velocity and wave-front curves have only been determined in detail for hexagonal and cubic materials. The simplest is the hexagonal system which belongs to the class of transversely isotropic solids, due to the circular symmetry around the hexagonal axis. For this type of anisotropy exact analytical solutions of the wave field have been calculated for homogeneous media only along the symmetry axis (3), and for the surface wave-motion problem of a point-loaded half-space (4) (Lamb's problem).

As mentioned before the type of transversely isotropic materials includes hexagonal crystals and also may be a very good representation of the earth's structure. The real earth is generally stratified with elastic properties and density which vary stepwise with increasing depth. If the dominant

† On leave from: Yacimientos Petroliferos Fiscales, Gerencia de Exploracion, Pte. R. S. Pena 777, 1364 Buenos Aires, Argentina. Present Address: Hamburg University, D-2000 Hamburg, Federal Republic of Germany.

wavelength of the wave field is long enough compared to the dimensions of these varying strata, an averaging effect takes place which leads to transverse isotropy. In the first case measurements of ultrasonic wave propagation are performed in order to determine the elasticities of crystals, and in the latter case information about the lithology of formations is extracted through the inversion of the seismograms.

Wave-propagation simulation has been advancing considerably in recent years (see, for example, Aboudi (5)). With the progress in new methods and new computer technology, it has become possible to solve the governing wave equation with a high degree of precision. This combined with significant advances in data quality suggests a strong need to develop an accurate algorithm for wave-propagation calculations in anisotropic media.

This paper considers two-dimensional wave propagation through a general heterogeneous transversely isotropic medium. To solve the equation of motion, a new time-integration technique is used. The method is very accurate and yet involves the same amount of computational effort as second-order finite differences in time. This new pseudospectral numerical scheme (6) has already been successfully applied to solving the acoustic (7) and Schrödinger (8) wave equations, and to the viscoacoustic (9) and viscoelastic (10) equations of motion.

The first section presents the constitutive relation of the transversely isotropic solid. Then the equation of motion for the two-dimensional case is derived, and the numerical algorithm is developed. The next section reviews some basic concepts about the velocity and wave-front curves in transversely isotropic materials, and finally examples of wave propagation are presented.

The numerical algorithm is tested against the problem of wave propagation in a homogeneous class IV transversely isotropic media.

## 2. Constitutive relations of the transversely isotropic medium

The constitutive relation of a heterogeneous anisotropic and elastic solid is expressed by the generalized Hooke's law, which can be written as

$$\sigma_{ij} = c_{ijkl}\varepsilon_{kl}, \quad i, j, k, l = 1, \dots, 3, \quad (2.1)$$

where  $t$  is the time,  $\mathbf{x}$  is the position vector,  $\sigma_{ij}(\mathbf{x}, t)$  and  $\varepsilon_{ij}(\mathbf{x}, t)$  are the Cartesian components of the stress and strain tensors respectively, and  $c_{ijkl}(\mathbf{x})$  are the components of a fourth-order tensor called the elasticities of the medium. The Einstein convention for repeated indices is used.

To express the stress-strain relation for a transversely isotropic medium we introduce a shortened matrix notation commonly used in the literature. With this convention, pairs of subscripts concerning the elasticities are replaced by a single number according to the following correspondence:

$$(11) \rightarrow 1, \quad (22) \rightarrow 2, \quad (33) \rightarrow 3, \quad (23) = (32) \rightarrow 4, \\ (31) = (13) \rightarrow 5, \quad (12) = (21) \rightarrow 6.$$

Using this convention, the constitutive relation for a transversely isotropic solid with symmetry axis coincident with the  $z$ -axis can be expressed as (2, p. 3),

$$\begin{bmatrix} \sigma_{11} \\ \sigma_{22} \\ \sigma_{33} \\ \sigma_{23} \\ \sigma_{31} \\ \sigma_{12} \end{bmatrix} = \begin{bmatrix} c_{11} & c_{12} & c_{13} & 0 & 0 & 0 \\ c_{12} & c_{11} & c_{13} & 0 & 0 & 0 \\ c_{13} & c_{13} & c_{33} & 0 & 0 & 0 \\ 0 & 0 & 0 & c_{44} & 0 & 0 \\ 0 & 0 & 0 & 0 & c_{44} & 0 \\ 0 & 0 & 0 & 0 & 0 & c_{66} \end{bmatrix} \begin{bmatrix} \epsilon_{11} \\ \epsilon_{22} \\ \epsilon_{33} \\ 2\epsilon_{23} \\ 2\epsilon_{31} \\ 2\epsilon_{12} \end{bmatrix}, \quad (2.2)$$

where  $c_{66} = \frac{1}{2}(c_{11} - c_{12})$ . The algorithm to solve the equation of motion of the anisotropic solid which is presented in the following section allows complete material variability. This means that the five independent elasticities in equation (2.2) can be space-dependent.

### 3. The equation of motion for a two-dimensional solid

In this work we consider wave propagation in a two-dimensional medium. Denoting  $x$  and  $z$  as the horizontal and vertical coordinates respectively, the stress-strain relation (2.2) can be written as

$$\begin{bmatrix} \sigma_{xx} \\ \sigma_{zz} \\ \sigma_{xz} \end{bmatrix} = \begin{bmatrix} c_{11} & c_{13} & 0 \\ c_{13} & c_{33} & 0 \\ 0 & 0 & c_{44} \end{bmatrix} \begin{bmatrix} \epsilon_{xx} \\ \epsilon_{zz} \\ 2\epsilon_{xz} \end{bmatrix}, \quad (3.1)$$

where the number of independent elasticities has been reduced from five in the three-dimensional solid to four in this case. Note that the constitutive relation for a medium with cubic symmetry is obtained as a special case by putting  $c_{33} = c_{11}$ , that is, only three independent elasticities remain.

The description of wave propagation is based on momentum conservation combined with the constitutive relation. The linearized equation of motion for a continuous medium is given by

$$\rho \ddot{\mathbf{u}} = \nabla \cdot \Sigma + \mathbf{f}, \quad (3.2)$$

where  $\mathbf{u}(\mathbf{x}, t)$  is the displacement field,  $\Sigma(\mathbf{x}, t)$  is the stress tensor,  $\mathbf{f}(\mathbf{x}, t)$  represents the body forces, and  $\rho(\mathbf{x})$  is the density. In equation (3.2) as in the remainder of the article, a dot above a variable denotes time differentiation.

For a two-dimensional solid, equation (3.2) can be expressed as

$$\rho \ddot{u}_x = \frac{\partial \sigma_{xx}}{\partial x} + \frac{\partial \sigma_{xz}}{\partial z} + f_x, \quad \rho \ddot{u}_z = \frac{\partial \sigma_{zx}}{\partial x} + \frac{\partial \sigma_{zz}}{\partial z} + f_z, \quad (3.3)$$

where  $u_x$  and  $u_z$ , and  $f_x$  and  $f_z$  are the components of the displacements and

body forces respectively. By replacing the constitutive relation (3.1) in the equations of motion (3.3), and making use of the strain–displacement relations (11, p. 13), we obtain

$$\left. \begin{aligned} \rho \ddot{u}_x &= \frac{\partial}{\partial x} \left[ c_{11} \frac{\partial u_x}{\partial x} + c_{13} \frac{\partial u_z}{\partial z} \right] + \frac{\partial}{\partial z} \left[ c_{44} \left( \frac{\partial u_x}{\partial z} + \frac{\partial u_z}{\partial x} \right) \right] + f_x, \\ \rho \ddot{u}_z &= \frac{\partial}{\partial z} \left[ c_{13} \frac{\partial u_x}{\partial x} + c_{33} \frac{\partial u_z}{\partial z} \right] + \frac{\partial}{\partial x} \left[ c_{44} \left( \frac{\partial u_x}{\partial z} + \frac{\partial u_z}{\partial x} \right) \right] + f_z. \end{aligned} \right\} \quad (3.4)$$

The equations of motion for an isotropic solid are a special case of equations (3.4) when  $c_{11} = c_{33} = \lambda + 2\mu$ ,  $c_{13} = \lambda$ , and  $c_{44} = \mu$ , where  $\lambda$  and  $\mu$  are the Lamé constants.

#### 4. Numerical algorithm

In order to solve the problem numerically we recast equations (3.4) as a coupled first-order equation in time as follows:

$$\dot{\mathbf{U}} = \mathbf{M}\mathbf{U} + \mathbf{F}, \quad (4.1)$$

where  $\mathbf{M}$  is a spatial operator matrix of dimension 4 given by

$$\mathbf{M} = \begin{bmatrix} 0 & 0 & 1 & 0 \\ 0 & 0 & 0 & 1 \\ M_{31} & M_{32} & 0 & 0 \\ M_{41} & M_{42} & 0 & 0 \end{bmatrix}, \quad (4.2)$$

with its components defined by

$$\left. \begin{aligned} M_{31} &= \frac{1}{\rho} \left( \frac{\partial}{\partial x} c_{11} \frac{\partial}{\partial x} + \frac{\partial}{\partial z} c_{44} \frac{\partial}{\partial z} \right), \\ M_{32} &= \frac{1}{\rho} \left( \frac{\partial}{\partial x} c_{13} \frac{\partial}{\partial z} + \frac{\partial}{\partial z} c_{44} \frac{\partial}{\partial x} \right), \\ M_{41} &= \frac{1}{\rho} \left( \frac{\partial}{\partial x} c_{44} \frac{\partial}{\partial z} + \frac{\partial}{\partial z} c_{13} \frac{\partial}{\partial x} \right), \\ M_{42} &= \frac{1}{\rho} \left( \frac{\partial}{\partial x} c_{44} \frac{\partial}{\partial x} + \frac{\partial}{\partial z} c_{33} \frac{\partial}{\partial z} \right) \end{aligned} \right\} \quad (4.3)$$

and

$$\mathbf{U}^T = [u_x, u_z, \dot{u}_x, \dot{u}_z], \quad (4.4)$$

with the source vector,

$$\mathbf{F}^T = [0, 0, f_x/\rho, f_z/\rho]. \quad (4.5)$$

After a spatial discretization in  $x$  and  $z$  and a suitable approximation for the spatial derivatives, equation (4.1) becomes a coupled system of

$4N \equiv 4N_x N_z$  ordinary differential equations in the unknowns  $u_x$ ,  $u_z$ ,  $\dot{u}_x$  and  $\dot{u}_z$  at the grid points. The numbers of grid points in the  $x$ - and  $z$ -directions are denoted by  $N_x$  and  $N_z$  respectively.

In this work we calculate the spatial-derivative terms by the Fourier pseudospectral method (12, 13), which consists of a spatial discretization and calculation of spatial derivatives using the fast Fourier transform (FFT). For instance, the quantity  $(\partial/\partial x)c_{13}(\partial u_z/\partial z)$  in equation (3.4)<sub>1</sub> is calculated in the following way. First, along each  $z$ -line a spatial FFT on  $u_z$  is performed. The result is then multiplied by the complex spatial-wave-number vector,

$$ik_v = \frac{2\pi i v}{N_z DZ}, \quad v = -\frac{1}{2}N_z, \dots, \frac{1}{2}N_z,$$

where  $DZ$  is the grid spacing in the  $z$ -direction and  $i^2 = -1$ . This operation is followed by an inverse FFT into the spatial domain yielding  $\partial u_z/\partial z$ , which is then multiplied by  $c_{13}$ . Then forward and inverse FFTs along each  $x$ -line are performed to calculate  $(\partial/\partial x)c_{13}(\partial u_z/\partial z)$ .

Equation (4.1) can be expressed in compact notation as

$$\dot{\mathbf{U}}_N = \mathbf{M}_N \mathbf{U}_N + \mathbf{F}_N, \quad (4.6)$$

subject to the initial conditions

$$\mathbf{U}_N(0) = \mathbf{U}_N^0, \quad (4.7)$$

where  $\mathbf{U}_N$ ,  $\mathbf{M}_N$  and  $\mathbf{F}_N$  are the discrete representations of  $\mathbf{U}$ ,  $\mathbf{M}$  and  $\mathbf{F}$  respectively. The solution to equation (4.6) subject to (4.7) is formally given by

$$\mathbf{U}_N = e^{\mathbf{M}_N t} \mathbf{U}_N^0 + \int_0^t e^{\mathbf{M}_N \tau} \mathbf{F}_N(t - \tau) d\tau. \quad (4.8)$$

We consider a separable source term  $\mathbf{F}_N(t) = \mathbf{A}_N h(t)$ , where  $\mathbf{A}_N$  is the spatial distribution of the source, usually chosen to be a delta or a highly localized function. The function  $h(t)$  is the source-time history. Considering zero initial condition and replacing the source term, equation (4.8) becomes

$$\mathbf{U}_N = \left[ \int_0^t e^{\mathbf{M}_N \tau} h(t - \tau) d\tau \right] \mathbf{A}_N. \quad (4.9)$$

To solve this equation we use a new time-integration technique based on the well-known Chebycheff expansion of the function  $e^z$  (6),

$$e^z \approx H_K(z) = \sum_{k=0}^K C_k J_k(\tau R) Q_k \left[ \frac{z}{\tau R} \right], \quad (4.10)$$

where  $|z| \leq \tau R$  and  $z$  lies close to the imaginary axis. Now  $C_0 = 1$  and  $C_k = 2$  for  $k \geq 1$ ,  $J_k$  is the Bessel function of order  $k$  and  $Q_k$  are the modified

Chebyshev polynomials which satisfy the recurrence relation

$$Q_{k+1}(s) = 2sQ_k(s) + Q_{k-1}(s), \quad (4.11)$$

with

$$Q_0 = 1 \quad \text{and} \quad Q_1 = s. \quad (4.12)$$

Substituting  $\tau \mathbf{M}_N$  for  $z$  in (4.10), equation (4.9) becomes

$$\mathbf{U}_N(t) \approx \mathbf{U}_N^K = \sum_{k=0}^K C_k b_k(tR) Q_k \left[ \frac{\mathbf{M}_N}{R} \right] \mathbf{A}_N, \quad (4.13)$$

where the coefficients  $b_k$  are given by

$$b_k = \int_0^t J_k(\tau R) h(t - \tau) d\tau. \quad (4.14)$$

The variable  $R$  must be chosen larger than the region spanned by the eigenvalues of  $\mathbf{M}_N$ , which should be in the vicinity of the imaginary axis (this is shown in Appendix A together with the determination of  $R$ ). Tal-Ezer (6) showed that the largest  $k = K$  in equation (4.13) should be greater than  $tR$  to ensure convergence. The actual value of  $K$  can be determined by finding the range in which the coefficients  $b_k$  are significantly different from zero.

The starting values for the recursion are given by

$$Q_0 \left[ \frac{\mathbf{M}_N}{R} \right] \mathbf{A}_N = \mathbf{A}_N \quad \text{and} \quad Q_1 \left[ \frac{\mathbf{M}_N}{R} \right] \mathbf{A}_N = \frac{\mathbf{M}_N}{R} \mathbf{A}_N, \quad (4.15)$$

according to equation (4.12). Additional terms are generated by (4.11) with  $\mathbf{M}_N/R$  replacing  $s$ , while  $\mathbf{U}_N^K$  is cumulated by (4.13). The final value of  $\mathbf{U}_N^K$  is obtained after cumulating  $K$  terms.

The solution can be propagated in time again by considering  $\mathbf{U}_N^K(t_0)$  as an initial condition, by means of the homogeneous solution in equation (4.8). This yields

$$\mathbf{U}_N(t) \approx \mathbf{U}_N^K = \sum_{k=0}^K C_k J_k(tR) Q_k \left[ \frac{\mathbf{M}_N}{R} \right] \mathbf{U}_N(t_0), \quad (4.16)$$

where  $t_0$  is the size of the first time increment which should be larger than the duration of the source time history. The calculation of time histories at a given point of the material does not require significant additional computational effort since the terms  $Q_k(\mathbf{M}_N/R) \mathbf{U}_N$  are calculated in any case; only additional sets of Bessel functions need to be generated. The intermediate results are calculated according to

$$\mathbf{U}_N(t') \approx \mathbf{U}_N^K = \sum_{k=0}^K C_k J_k(t'R) Q_k \left[ \frac{\mathbf{M}_N}{R} \right] \mathbf{U}_N(t_0) \quad (4.17)$$

for  $t' < t$ .

Because the Fourier pseudospectral method considers the discretized variables on the grid as periodic functions, absorbing boundaries are implemented to prevent wrap-around, the phenomenon in which a pulse which leaves the grid on one side re-enters it on the opposite side. To eliminate this effect from the boundaries of the numerical grid, we use a method developed by Kosloff and Kosloff (14). The absorbing boundary is performed through a systematic elimination of the wave amplitude in a strip along the boundary of the grid. This is achieved by replacing the operator  $\mathbf{M}$  in equation (4.1) by the operator  $(\mathbf{M} - \alpha\mathbf{I})$ , where  $\mathbf{I}$  is the identity matrix and  $\alpha$ , which determines the absorption, is given by

$$\alpha = U_0/\cosh^2(\delta m), \quad (4.18)$$

where  $U_0$  is a constant and  $\delta$  is a decay factor. The parameter  $\alpha(x, z)$  is chosen in order that it differs from zero only in a strip of nodes ( $m$ ) surrounding the numerical mesh.

Equation (4.18) has the functional form of the complex potentials used in quantum mechanics, where with an appropriate choice of the parameters it is possible to eliminate reflected or transmitted energy from the absorbing region. The spatial dependence of  $\alpha(x, z)$  is chosen to give the best amplitude elimination.

To clarify the method we consider the one-dimensional version of equation (4.1) with constant material properties and zero source term,

$$\frac{d}{dt} \begin{bmatrix} u_x \\ V \end{bmatrix} = \begin{bmatrix} -\alpha & 1 \\ c^2 \frac{\partial}{\partial x^2} & -\alpha \end{bmatrix} \begin{bmatrix} u_x \\ V \end{bmatrix}, \quad (4.19)$$

where  $c$  is the wave velocity. When  $\alpha = 0$ , the first equation in (4.19) expresses the relation  $V = du_x/dt$ , whereas the second one is the acoustic wave equation. With the inclusion of the parameter  $\alpha$  and eliminating the variable  $V$ , equation (4.19) reads

$$\ddot{u}_x = c^2 \frac{d^2 u_x}{dx^2} - 2\alpha \dot{u}_x - \alpha^2 u_x. \quad (4.20)$$

This equation has a general solution of the form

$$u_x(x, t) = Af_1(x - ct)e^{-(\alpha/c)x} + Bf_2(x + ct)e^{(\alpha/c)x}, \quad (4.21)$$

with  $A$  and  $B$  arbitrary constants and  $f_1$  and  $f_2$  arbitrary twice-differentiable functions. The solution represents attenuating waves in space, where all frequency components are equally attenuated. This means that the absorbing boundary will gradually attenuate the wave field without changing its shape or producing dispersion.

### 5. The velocity and wave-front curves in a homogeneous medium

The normal curve for a transversely isotropic solid is defined by the following parametric form (2, p. 17):

$$p = R_{\pm}(\theta) \cos \theta \quad \text{and} \quad q = R_{\pm}(\theta) \sin \theta, \quad (5.1)$$

where

$$R_{\pm}(\theta) = \left[ \frac{B(\theta) \pm (B^2(\theta) - 4A(\theta))^{\frac{1}{2}}}{2A(\theta)} \right]^{\frac{1}{2}}, \quad (5.2)$$

with

$$\left. \begin{aligned} A(\theta) &= \alpha \cos^4 \theta + \gamma \cos^2 \theta \sin^2 \theta + \beta \sin^4 \theta, \\ B(\theta) &= (\alpha + 1) \cos^2 \theta + (\beta + 1) \sin^2 \theta. \end{aligned} \right\} \quad (5.3)$$

The parameters  $\alpha$ ,  $\beta$  and  $\gamma$  in equations (5.3) are given by

$$\alpha = c_{33}/c_{44}, \quad \beta = c_{11}/c_{44}, \quad \gamma = 1 + \alpha\beta - (c_{13}/c_{44} + 1)^2. \quad (5.4)$$

The velocity curve is the inverse of the normal curve and is defined parametrically by

$$v_{x_{\pm}} = V_{\pm}(\theta) \sin \theta \quad \text{and} \quad v_{z_{\pm}} = V_{\pm}(\theta) \cos \theta, \quad (5.5)$$

with

$$V_{\pm}(\theta) = V_S/R_{\pm}(\theta), \quad (5.6)$$

and

$$V_S = (c_{44}/\rho)^{\frac{1}{2}} \quad (5.7)$$

is a reference wave velocity of the medium, which in a transversely isotropic medium corresponds to the vertical and to the horizontal pure transverse wave velocity (15).

The velocity curve consists of two branches differentiated by the sign in (5.5). Under the condition of strict hyperbolicity (2, p. 18) we must have

$$V_+(\theta) < V_-(\theta). \quad (5.8)$$

The velocity curve defined by the minus sign in (5.5) corresponds to the quasilongitudinal mode, and that defined by the plus sign to the quasi-transverse mode. The displacement amplitudes corresponding to these modes are always orthogonal, but not perpendicular or coincident with the wave front as in the isotropic solid. In seismology these modes represent the P and SV wave fronts, but actually the waves are purely compressional or shear only when the direction of propagation is perpendicular to ( $V_P = (c_{11}/\rho)^{\frac{1}{2}}$ ), or coincident with ( $V_P = (c_{33}/\rho)^{\frac{1}{2}}$ ) the symmetry axis of the transversely isotropic solid (15).

The wave-front curve, which is constructed as the envelope of plane waves at a given time  $t$ , consists also of two branches defined parametrically



by (2, p. 35),

$$\left. \begin{aligned} z_{\pm} &= \frac{V_{\pm} t \cos \theta}{2A} \left[ 2\alpha \cos^2 \theta + \gamma \sin^2 \theta \pm \frac{\sin^2 \theta (k_1 \cos^2 \theta - k_2 \sin^2 \theta)}{(B^2 - 4A)^{\frac{1}{2}}} \right], \\ x_{\pm} &= \frac{V_{\pm} t \sin \theta}{2A} \left[ 2\beta \sin^2 \theta + \gamma \cos^2 \theta \mp \frac{\cos^2 \theta (k_1 \cos^2 \theta - k_2 \sin^2 \theta)}{(B^2 - 4A)^{\frac{1}{2}}} \right], \end{aligned} \right\} \quad (5.9)$$

where  $k_1 = 2\alpha(\beta + 1) + \gamma(\alpha + 1)$  and  $k_2 = 2\beta(\alpha + 1) - \gamma(\beta + 1)$ .

The normal and wave-front curves in transversely isotropic materials are classified according to the existence and location of inflexion points and cusps respectively (2, pp. 26, 38). The existence of inflexion points in the normal curve gives rise to lacunae or cusps in the wave-front curve.

It is important to point out that there is no simple correspondence between the velocity and wave-front curves. The velocity  $V_{\pm}(\theta)$  measures the velocity of advance of the wave front along the wave-number vector  $\mathbf{k}(\theta)$ , which is normal to the wave-front curve. Given a point  $P = (x_0, z_0)$  on this curve, the corresponding point  $Q = (v_{x_0}, v_{z_0})$  is obtained by passing through the origin a line parallel to the direction of the vector  $\mathbf{k}$  and intersecting the velocity curve (15). Only for spherical wave fronts (isotropic case) will the points  $P$  and  $Q$  lie on the same radial line.

## 6. Wave-propagation simulation

Now we examine wave propagation through different materials (homogeneous and heterogeneous), and test the numerical algorithm against the analytical solution along the symmetry axis.

### 6.1 Wave fronts in three different hexagonal crystals

The motion is initiated by a  $z$ -directional point force located at the centre of a  $165 \times 165$  grid with spacing  $DX = DZ = 0.2$  cm. The source is a shifted zero-phase pulse defined by

$$F(t) = e^{-0.5f_0^2(t-t_0)^2} \cos \pi f_0(t - t_0), \quad (6.1)$$

with  $t_0 = 6 \mu\text{s}$  and a high cut-off frequency  $f_0 = 5 \times 10^5$  Hz. No absorbing boundaries are used in this case because the perturbation does not exceed the grid limits.

Table 1 shows the elasticity constants and densities of the three materials. The last column presents the time at which the snapshots are calculated. The materials are classified according to the existence and location of inflexion points in the normal curve or, equivalently, of cusps in the wave-front curve.

Figures 1 and 2, and 3 and 4 show the velocity curves, wave-front curves and snapshots of the three crystals, respectively (a) for apatite, (b) for zinc, and (c) for cobalt. Figures 3 represent the  $u_x$ -components of the wave front

TABLE 1. *Material properties of the hexagonal crystals*

| Crystal | Class | $c_{11}$ | $c_{13}$ | $c_{33}$ | $c_{44}$ | Density<br>( $\text{gr cm}^{-3}$ ) | Time<br>( $\mu\text{s}$ ) |
|---------|-------|----------|----------|----------|----------|------------------------------------|---------------------------|
| Apatite | IV    | 16.7     | 6.6      | 14.0     | 6.63     | 3.2                                | 20                        |
| Zinc    | IV    | 16.5     | 5.0      | 6.2      | 3.96     | 7.1                                | 32                        |
| Cobalt  | V     | 30.7     | 10.3     | 35.8     | 7.55     | 8.9                                | 24                        |

The elasticities should be multiplied by  $10^{11}$  dyne  $\text{cm}^{-2}$ .

and Figs 4, the  $u_x$ -components. The velocity and wave-front curves have the corresponding inflexion points and cusps, respectively, according to the classification given by Payton (2, pp. 26, 38). The cuspidal triangles around  $z_{\pm} = 0$  in zinc cannot be seen because they are too small.

All the wave fronts show the characteristics predicted by the respective wave-front curves, with the quasilongitudinal mode weaker than the quasitransverse mode. It can be seen also that the  $u_x$ -component along the symmetry axis is zero, in agreement with the theoretical solution given by equation (B.3).

Due to symmetry considerations, the  $u_x$  wave fronts should show

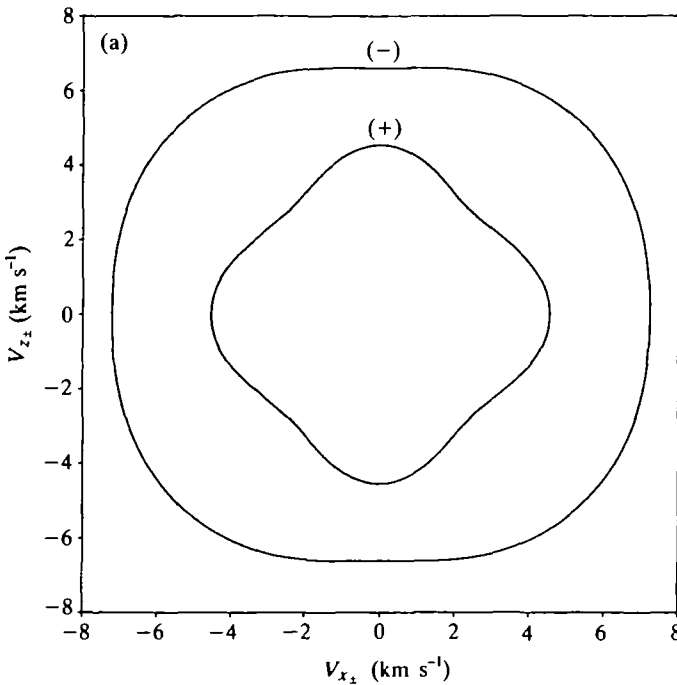


FIG. 1. Velocity curves for (a) apatite, (b) zinc, and (c) cobalt. The minus sign corresponds to the quasilongitudinal mode, and the plus sign to the quasitransverse mode

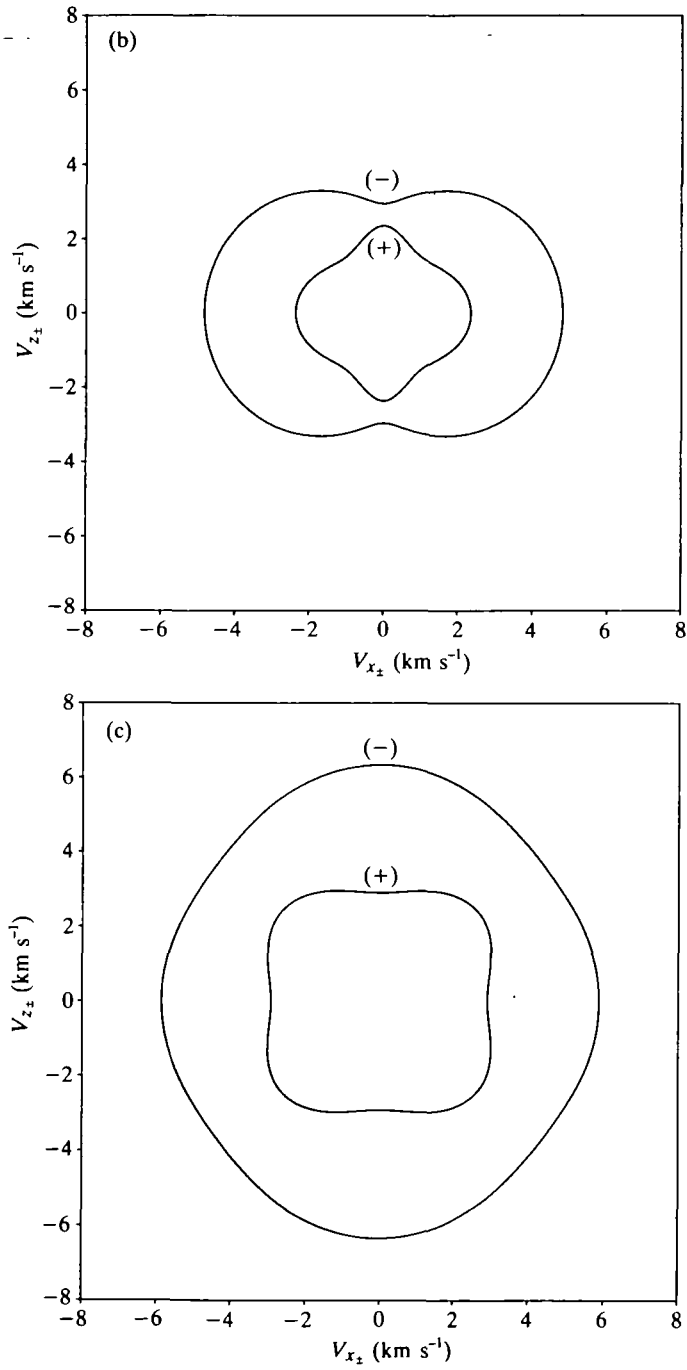


FIG. 1. (Continued)

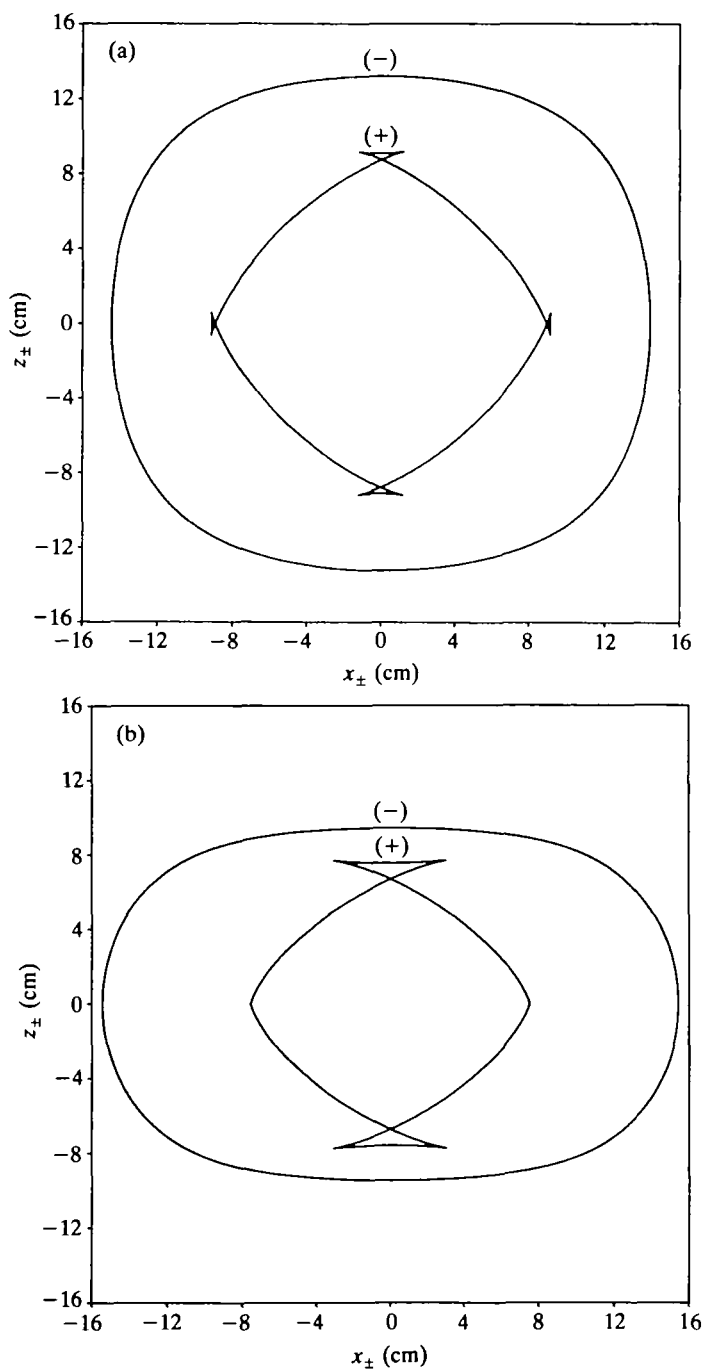


FIG. 2. Wave-front curves for (a) apatite, (b) zinc, and (c) cobalt. The minus sign corresponds to the quasilongitudinal mode, and the plus sign to the quasitransverse mode

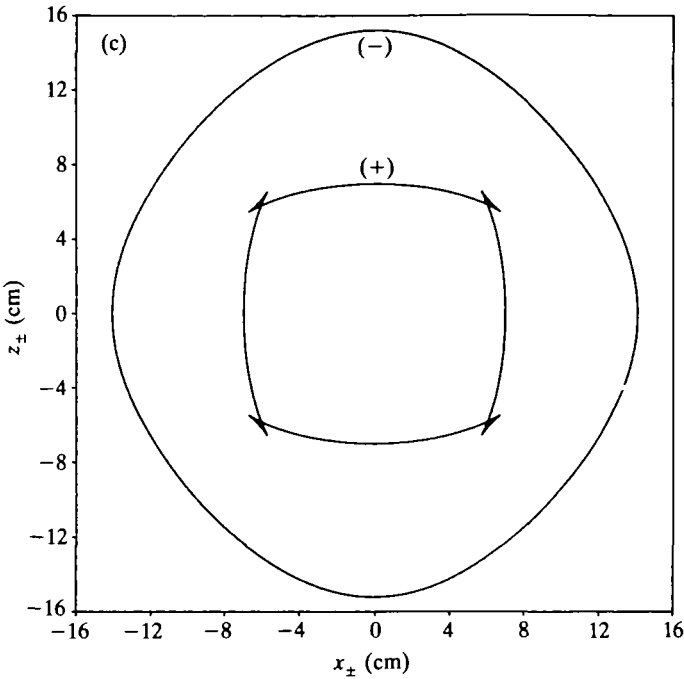


FIG. 2. (Continued)

antisymmetric behaviour across  $x = 0$  and  $z = 0$ , and the  $u_z$  wave fronts show symmetric behaviour across the same lines. The effects can be visualized for both components across  $z = 0$ , but because of the nature of the display, these are not evident across  $x = 0$ . A careful analysis reveals that equidistant points at both sides of the line  $x = 0$  for the  $u_x$  wave fronts have the same amplitude but opposite sign (antisymmetry). The same analysis shows that the  $u_z$  wave fronts are symmetric across  $x = 0$ .

### 6.2 Wave propagation in a heterogeneous material

This example considers wave propagation in a region consisting of two materials (Fig. 5). The left half-space is zinc and the right half-space is an isotropic solid with the following properties:

$$c_{11} = 16.5, \quad c_{33} = 16.5, \quad c_{13} = 8.58, \quad c_{44} = 3.96, \quad \rho = 7.1 \text{ gr cm}^{-3},$$

where the elasticities should be multiplied by  $10^{11}$  dyne  $\text{cm}^{-2}$ . This solid can be considered as an isotropic zinc, because the compressional and shear-wave velocities corresponds to the pure longitudinal (horizontal direction) and pure transverse wave velocities in zinc.

The simulation uses the grid parameters and pulse function of the previous example, but the source position is shifted from the centre of the

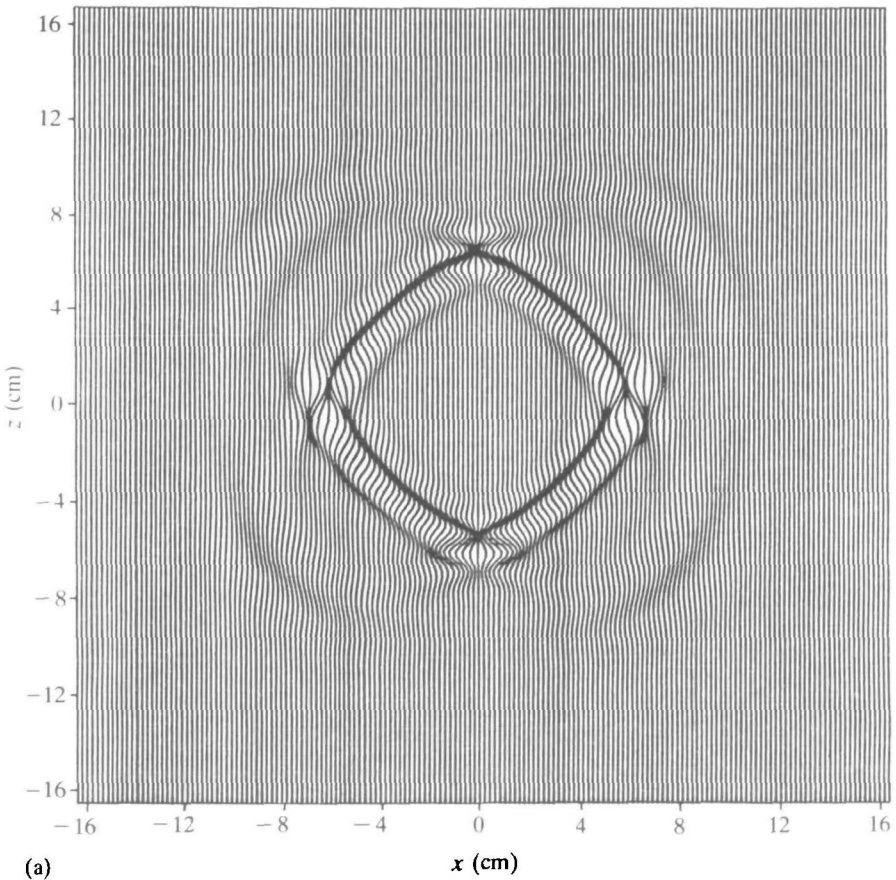


FIG. 3.  $u_x$ -components of the wave front for (a) apatite, (b) zinc, and (c) cobalt, due to a  $z$ -directional point force

grid (it is indicated by S in Fig. 5b). Snapshots of the wave field at  $t = 32 \mu\text{s}$  after the excitation of the source are shown in Figs 5a ( $u_x$ -component) and 5b ( $u_z$ -component). The main wave fronts present the expected characteristics of zinc (see Figs 3b and 4b) in the left half-space, and of an isotropic solid (concentric circles) in the right half-space.

A detailed interpretation of the snapshots allows the identification of the following events.

- (A) Primary quasilongitudinal wave.
- (B) Primary quasitransverse wave.
- (C) Reflected quasitransverse wave.
- (D) Converted quasitransverse wave generated by reflection of A.
- (E) Head wave which connects A with the transmitted longitudinal wave H.

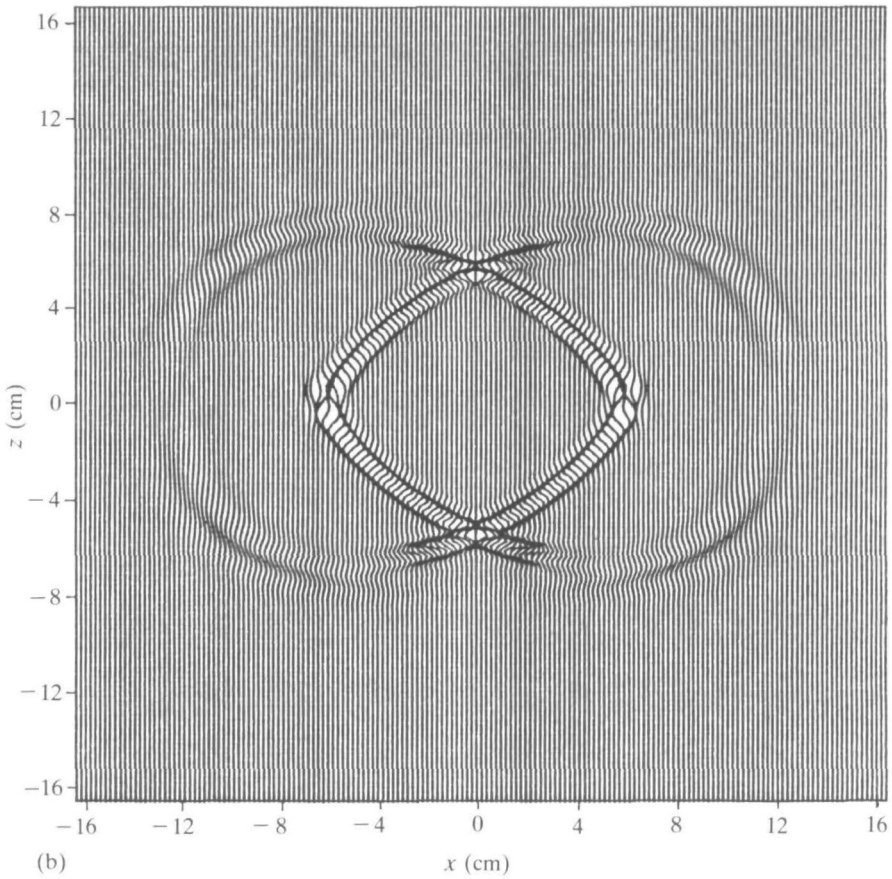


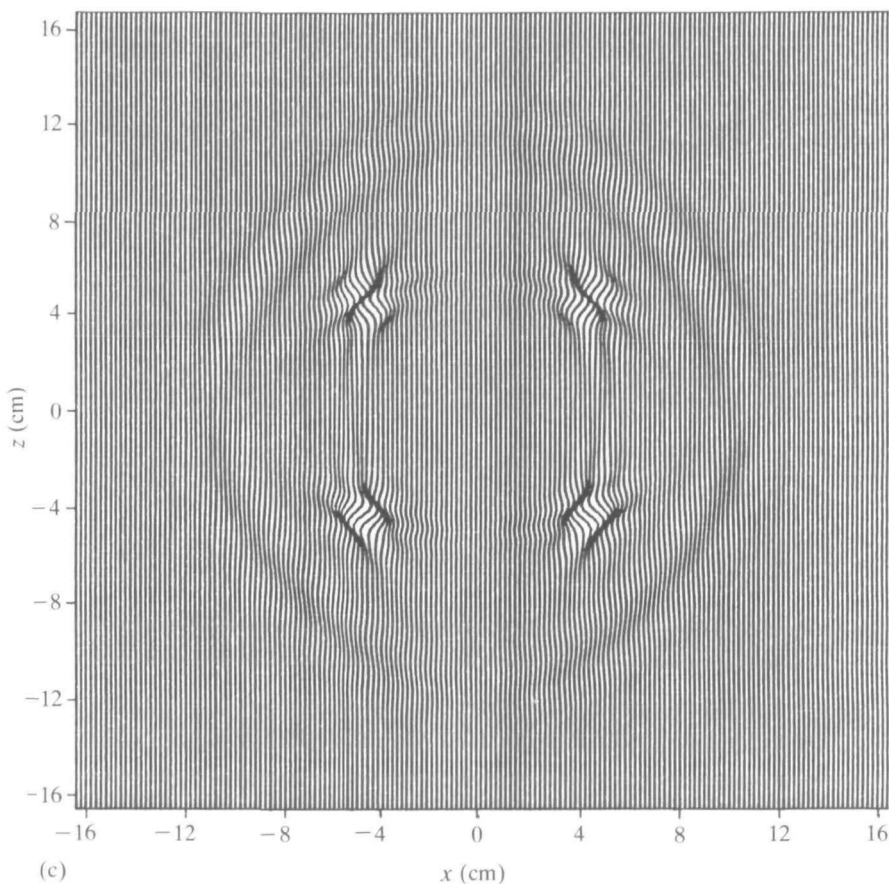
FIG. 3. (Continued)

- (F) Reflected quasilongitudinal wave.
- (G) Converted quasilongitudinal wave generated by reflection of B.
- (H) Transmitted longitudinal wave.
- (I) Transmitted transverse wave.
- (J) Transmitted transverse wave generated by the cusps.
- (K) Converted transverse wave generated by transmission of A.

The application shows how the model can handle the large number of phenomena present in heterogeneous materials, even the small-amplitude head-wave fronts.

### 6.3 Comparison with analytical results

In class IV transversely isotropic media the wave-front curve has four cuspidal triangles, two centred on the  $z_+$ -axis, and two centred on the

FIG. 3. (*Continued*)

$x_+$ -axis. In the apatite, as can be seen from Fig. 2a, a line drawn very close to the axis of symmetry, for example, intersects the wave-front curve in four points. This means that a single pulse at the origin will produce four separated pulses of energy.

The analytical solution in the symmetry axis for an homogeneous solid is given in Appendix B. In Fig. 6 is represented the apatite free-space Green's function (equation (B.5)) at a distance of  $z = 8$  cm from the source position. The singularities are located at times  $t_p$  and  $t_1$  respectively and the lacuna can be seen between times the  $t_s$  and  $t_1$  (the times are defined by equations (B.6)). The last singularity is not present in an isotropic medium because substitution of equations (5.4) in (B.7) gives  $\bar{z}_1 = 0$ , which by (B.6) implies that  $t_1 \rightarrow \infty$ .

The numerical model uses a  $99 \times 99$  grid with a spacing of  $DX = DZ = 0.2$  cm. The source time history of the previous examples is used.



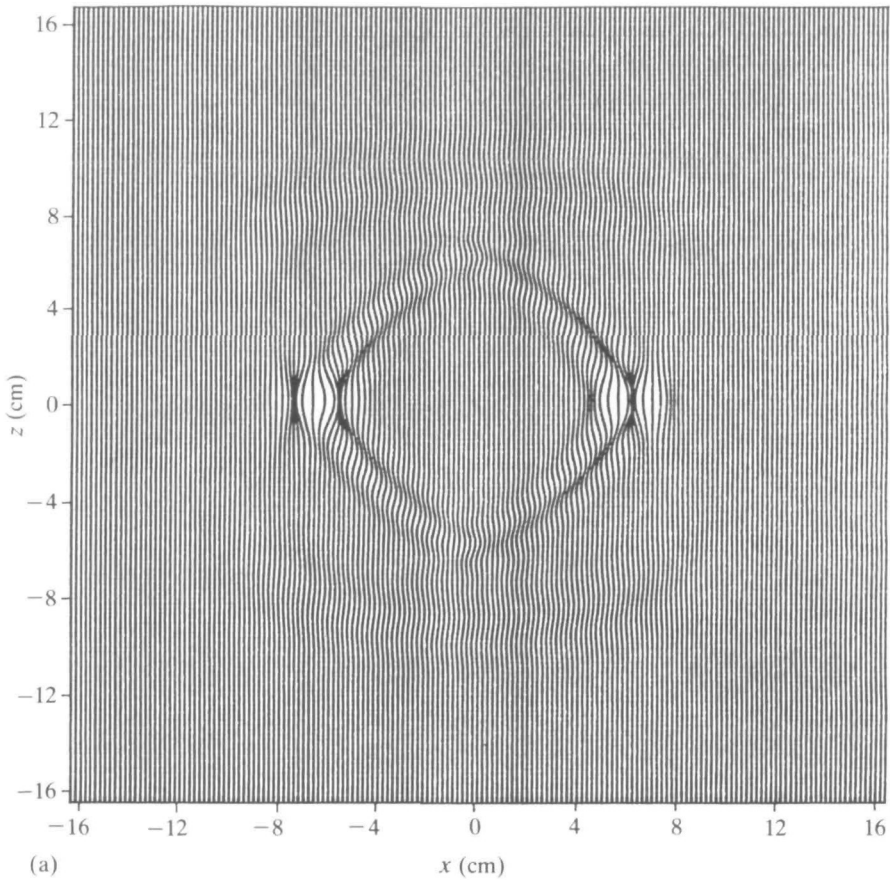


FIG. 4.  $u_z$ -components of the wave front for (a) apatite, (b) zinc, and (c) cobalt, due to a  $z$ -directional point force

Figures 7a and 7b compare numerical and analytical solutions at distances of 2.6 and 8 cm from the source position respectively. As the figures show, the comparison between numerical and analytical solutions is excellent.

## 7. Conclusions

This work has dealt with wave-propagation simulation in a two-dimensional transversely isotropic solid. The equations of motion are solved using a new pseudospectral numerical scheme in time. The method is based on the approach introduced by Tal-Ezer (6), in which the evolution operator is expanded in a Chebycheff polynomial series. Wave fronts calculated by the simulation algorithm show the characteristics predicted by the respective wave-front curves. The theory has been tested successfully

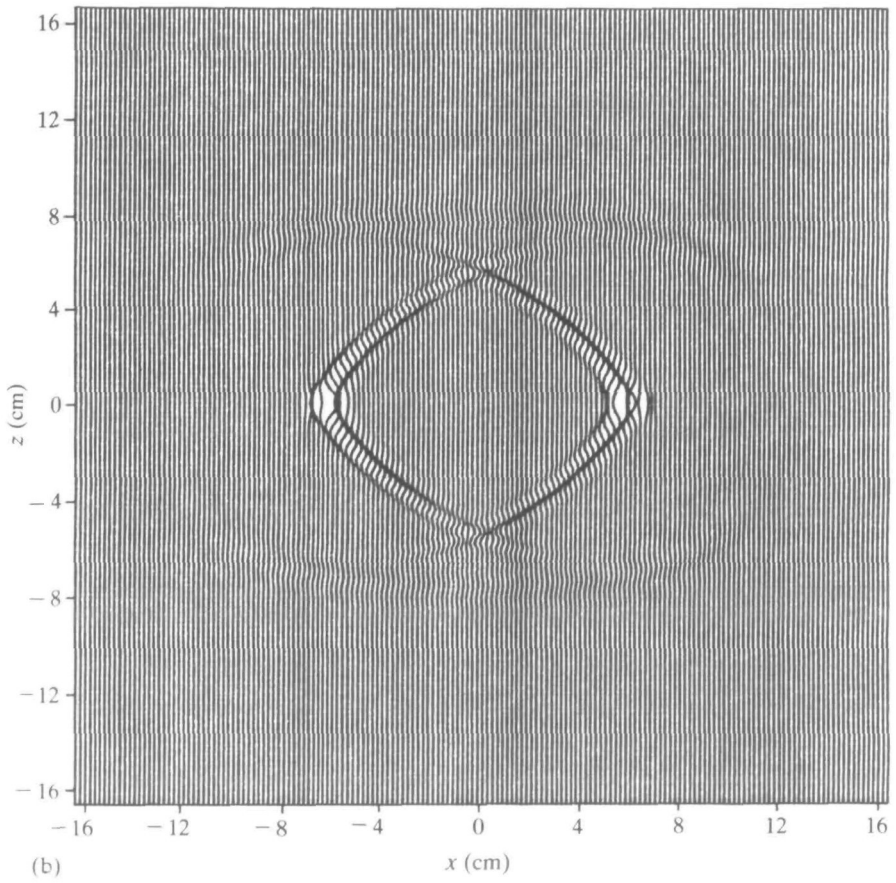


FIG. 4. (Continued)

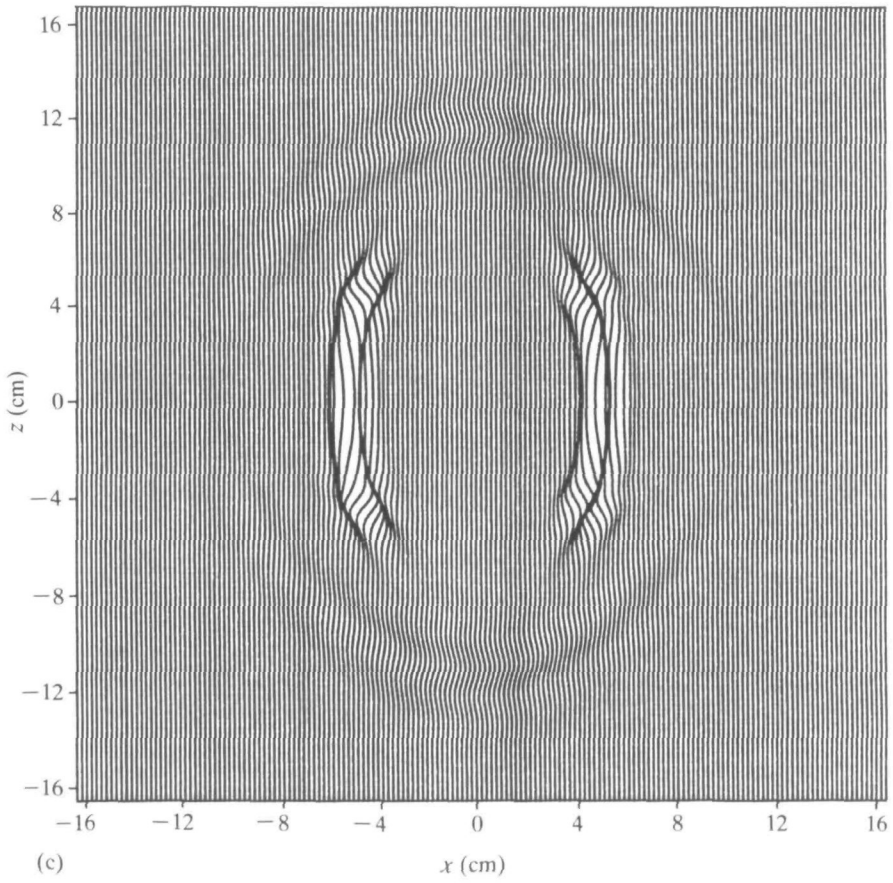


FIG. 4. (Continued)

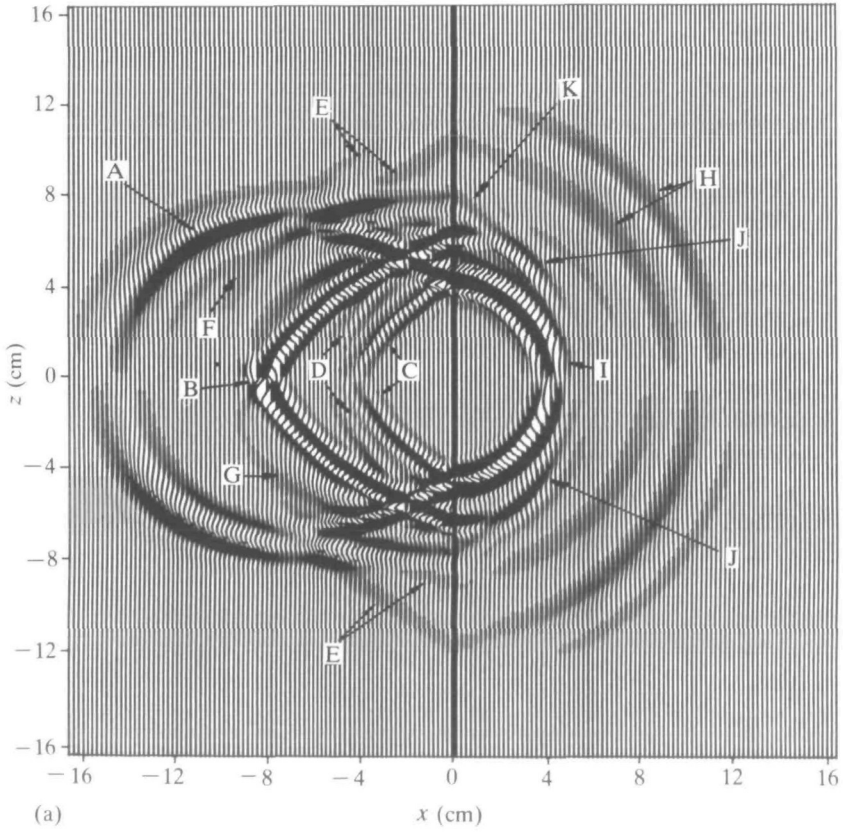


FIG. 5. Snapshots at  $t = 32\mu\text{s}$  for a heterogeneous material composed of zinc (left half-space) and an isotropic solid (right half-space); (a)  $u_x$ -component, (b)  $u_z$ -component

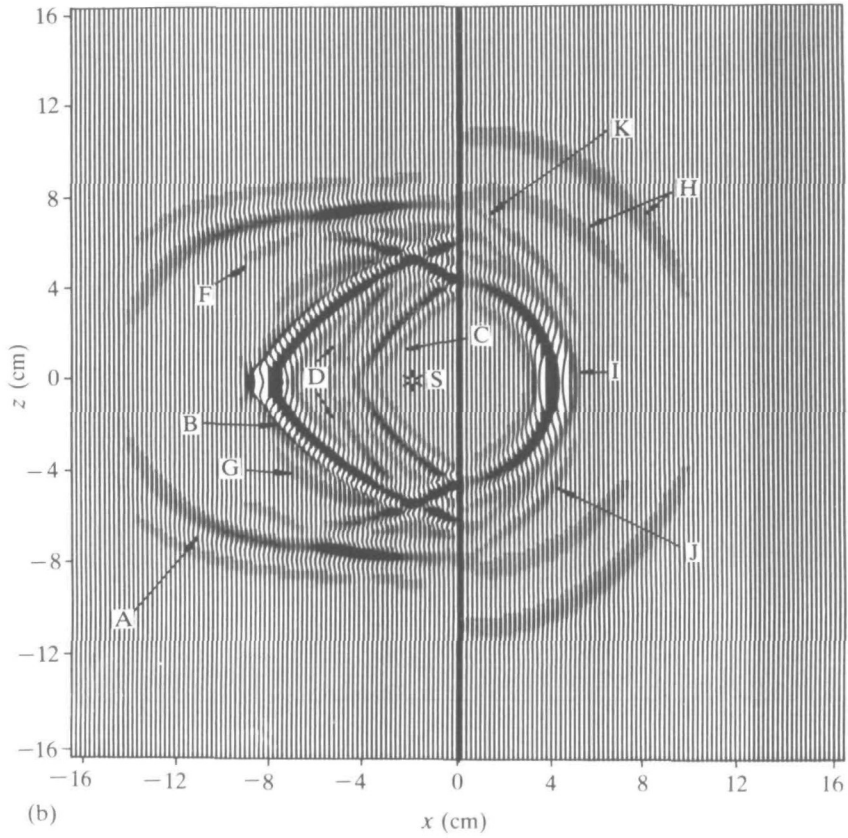


FIG. 5. (Continued)

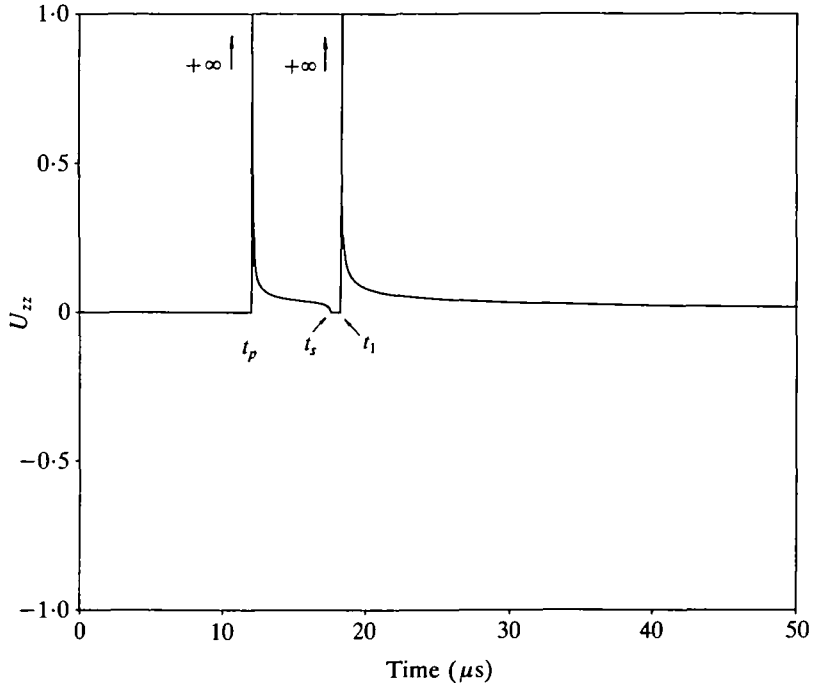


FIG. 6. Free-space Green's function ( $u_{zz}(x, t)$ ) due to a z-directional point force versus time in apatite, at a distance of 8 cm from the source position

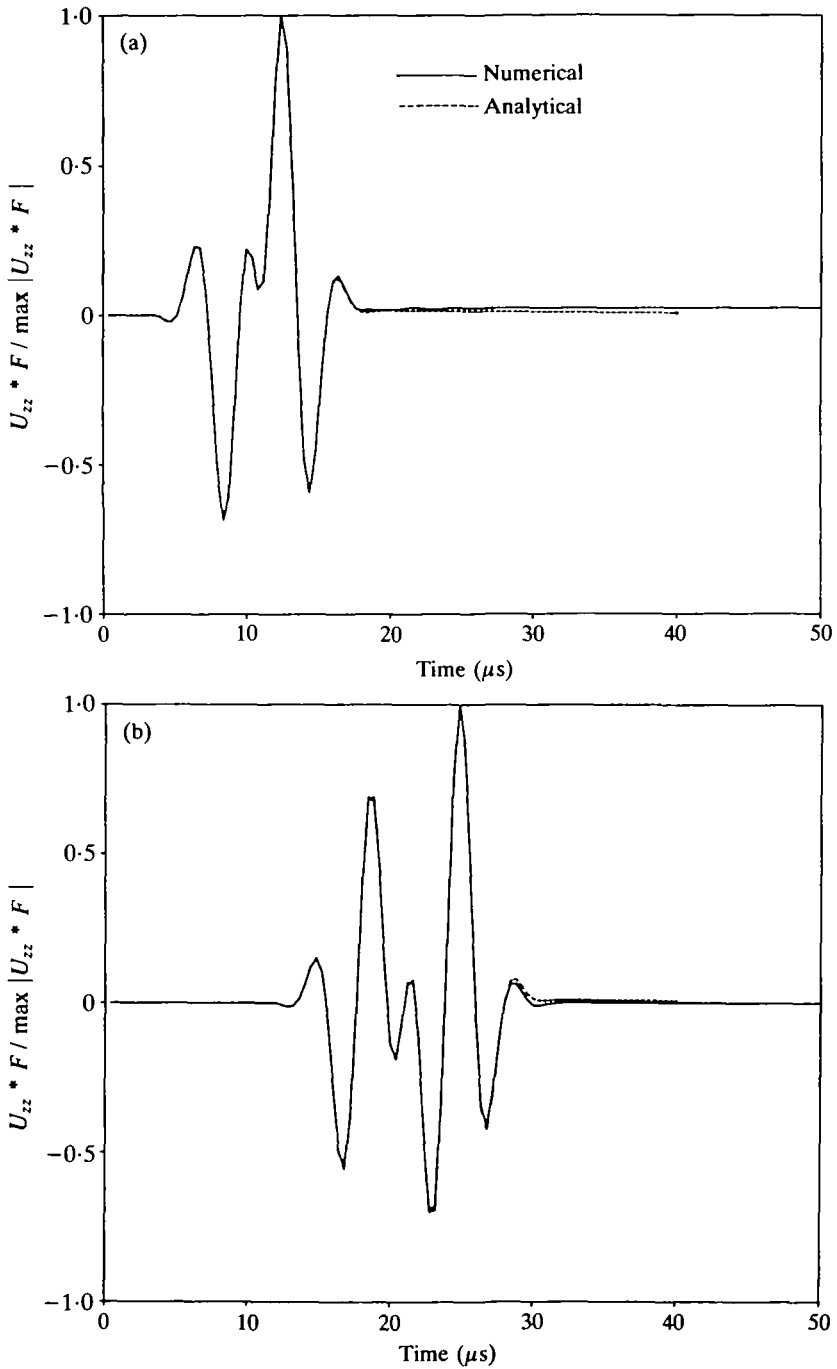


FIG. 7. Time-history comparison between the numerical and analytical solutions in the symmetry axis (time convolution of  $u_{zz}(t)$  with  $F(t)$ ) at distances of (a) 2.6 cm and (b) 8 cm from the source position, due to a  $z$ -directional point force. The medium is apatite

also when the medium is heterogeneous. The accuracy of the algorithm was verified in the comparison with the analytical solution in the symmetry axis of the material. The present numerical simulation can be very important in determining the solution of elastodynamic problems when the analytical solutions are either very complicated or unknown. Possible applications include realistic simulation of wave propagation through the earth, as well as in the field of material science. Extension of the algorithm to problems involving wave propagation in materials of different symmetry will be carried out in a future work.

### Acknowledgement

This work was partially supported by a research project on three-dimensional seismic modelling conducted jointly between the University of Hamburg and Tel Aviv University under contract 03E-6424-A of the BMFT, Federal Republic of Germany, and contract EN3C-0008-D of the European Community Commission.

### REFERENCES

1. M. J. P. MUSGRAVE, *Crystal Acoustics* (Holden-Day, San Francisco 1970).
2. R. G. PAYTON, *Elastic Wave Propagation in Transversely Isotropic Media* (Martinus Nijhoff, The Hague 1983).
3. R. G. PAYTON, *Z. angew. Math. Phys.* **29** (1978) 262–272.
4. R. BURRIDGE, *Q. Jl Mech. appl. Math.* **24** (1971) 81–98.
5. J. ABOUDI, *Modern Problems in Elastic Wave Propagation* (eds J. Miklowitz and J. D. Achenbach; Wiley, New York 1977) 45–65.
6. H. TAL-EZER, *SIAM J. numer. Anal.* **23** (1986) 11–26.
7. —, D. KOSLOFF and Z. KOREN, *Geophys. Prosp.* **35** 479–490.
8. — and R. KOSLOFF, *J. Chem. Phys.* **81** (1984) 3967–3971.
9. J. M. CARCIONE, D. KOSLOFF and R. KOSLOFF, unpublished.
10. —, — and —, unpublished.
11. K. AKI and P. G. RICHARDS, *Quantitative Seismology, Theory and Methods* (Freeman, San Francisco 1980).
12. B. FORNBERG, *SIAM J. numer. Anal.* **12** (1975) 509–528.
13. D. KOSLOFF and E. BAYSAL, *Geophysics* **47** (1982) 1402–1412.
14. — and R. KOSLOFF, *J. Comp. Phys.* **63** (1986) 363–376.
15. G. W. POSTMA, *Geophysics* **20** (1955) 780–806.

### APPENDIX A

#### *Eigenvalues of the propagation matrix and determination of R*

A plane-wave solution to equation (4.1) is assumed of the form

$$\mathbf{U} = \mathbf{U}_0 e^{i(\omega t - \mathbf{k} \cdot \mathbf{x})}, \quad (\text{A.1})$$

where  $\omega$  is the angular frequency,  $\mathbf{k}$  is the wave-number vector given by  $\mathbf{k} = (k_x, k_z)$ , and  $\mathbf{x}$  is the position vector. Considering constant elasticities and density and a zero



source term, substitution of (A.1) in equation (4.1) yields

$$i\omega \mathbf{U} = \begin{bmatrix} 0 & 0 & 1 & 0 \\ 0 & 0 & 0 & 1 \\ \bar{M}_{31} & \bar{M}_{32} & 0 & 0 \\ \bar{M}_{41} & \bar{M}_{42} & 0 & 0 \end{bmatrix} \mathbf{U}, \tag{A.2}$$

where the spatial double Fourier transform of the components of  $\mathbf{M}$  are given by

$$\left. \begin{aligned} \bar{M}_{31} &= -\frac{c_{11}k_x^2 + c_{44}k_z^2}{\rho}, \\ \bar{M}_{32} = \bar{M}_{41} &= -\frac{(c_{13} + c_{44})k_x k_z}{\rho}, \\ \bar{M}_{42} &= -\frac{c_{44}k_x^2 + c_{33}k_z^2}{\rho}. \end{aligned} \right\} \tag{A.3}$$

Equation (A.2) forms an eigenvalue equation for the eigenvalues  $\lambda_i = i\omega$ ,  $i = 1, \dots, 4$ . The characteristic equation of (A.2) is given by

$$\lambda_i^4 - (\bar{M}_{31} + \bar{M}_{42})\lambda_i^2 + (\bar{M}_{31}\bar{M}_{42} - \bar{M}_{41}\bar{M}_{32}) = 0. \tag{A.4}$$

For a transversely isotropic solid the constraints on the elasticities are as follows:  $c_{11}, c_{33}, c_{44} > 0$ ;  $|c_{13} + c_{44}| < [(c_{11}c_{33})^{1/2} + c_{44}]$  (2, p. 11). Thus  $B = -(\bar{M}_{31} + \bar{M}_{42}) > 0$ ,  $C = (\bar{M}_{31}\bar{M}_{42} - \bar{M}_{41}\bar{M}_{32}) > 0$  and  $B^2 - 4C > 0$ . With these conditions the roots of equation (A.4) lie on the imaginary axis. The eigenvalues are

$$\left. \begin{aligned} \lambda_1 &= \frac{i}{2^{\frac{1}{2}}} [|\bar{M}_{31} + \bar{M}_{42}| + [(\bar{M}_{31} - \bar{M}_{42})^2 + 4\bar{M}_{41}\bar{M}_{32}]^{\frac{1}{2}}]^{\frac{1}{2}}, & \lambda_2 &= -\lambda_1, \\ \lambda_3 &= \frac{i}{2^{\frac{1}{2}}} [|\bar{M}_{31} + \bar{M}_{42}| - [(\bar{M}_{31} - \bar{M}_{42})^2 + 4\bar{M}_{41}\bar{M}_{32}]^{\frac{1}{2}}]^{\frac{1}{2}}, & \lambda_4 &= -\lambda_3. \end{aligned} \right\} \tag{A.5}$$

For an isotropic solid, equations (A.3) become

$$\left. \begin{aligned} \bar{M}_{31} &= -\frac{(\lambda + 2\mu)k_x^2 + \mu k_z^2}{\rho}, \\ \bar{M}_{32} = \bar{M}_{41} &= -\frac{(\lambda + \mu)}{\rho} k_x k_z, \\ \bar{M}_{42} &= -\frac{\mu k_x^2 + (\lambda + 2\mu)k_z^2}{\rho}. \end{aligned} \right\} \tag{A.6}$$

Substitution of these expressions in equations (A.5) yields

$$\left. \begin{aligned} \lambda_1^{(0)} &= i\left(\frac{\lambda + 2\mu}{\rho}\right)(k_x^2 + k_z^2)^{\frac{1}{2}}, & \lambda_2^{(0)} &= -\lambda_1^{(0)}, \\ \lambda_3^{(0)} &= i\left(\frac{\mu}{\rho}\right)(k_x^2 + k_z^2)^{\frac{1}{2}}, & \lambda_4^{(0)} &= -\lambda_3^{(0)}. \end{aligned} \right\} \tag{A.7}$$

The first and second eigenvalues correspond to longitudinal wave propagation, and the third and fourth to shear wave propagation. They define the dispersion relations

$$\omega = v_p(k_x^2 + k_z^2)^{\frac{1}{2}} \quad \text{and} \quad \omega = v_s(k_x^2 + k_z^2)^{\frac{1}{2}}, \tag{A.8}$$

for longitudinal and shear waves respectively, where  $v_p = ((\lambda + 2\mu)/\rho)^{1/2}$ , and  $v_s = (\mu/\rho)^{1/2}$ .

Similarly, for a transversely isotropic solid,  $\lambda_1 = i\omega$  and  $\lambda_3 = i\omega$  define the dispersion relations. Note that substitution of the parametric form

$$k_x = k(\theta) \sin \theta, \quad k_z = k(\theta) \cos \theta \quad (\text{A.9})$$

in the dispersion relations yields  $k_{\pm}(\theta) = \omega/V_{\pm}(\theta)$ , where  $V_{\pm}(\theta)$  is the phase velocity (5.6). A numerical evaluation of the dispersion relations reveals that  $|\lambda_1(\theta)| = V_-(\theta)$  (quasilongitudinal mode), and  $|\lambda_3(\theta)| = V_+(\theta)$  (quasitransverse mode). This can also be deduced from the isotropic limit, equations (A.7).

The range of the eigenvalues of the propagation matrix,  $R$ , is obtained by substitution of  $k_x^N = \pi/DX$  and  $k_z^N = \pi/DZ$  (the Nyquist wave numbers give the highest eigenvalues) in equations (A.5). For the isotropic case we obtain

$$R^{(i)} = \pi v_p \left( \frac{1}{DX^2} + \frac{1}{DZ^2} \right)^{1/2}, \quad (\text{A.10})$$

using the fact that  $v_p > v_s$ , while for a transversely isotropic solid,  $R$  is given by

$$R = |\lambda_1(k_x^N, k_z^N)|, \quad (\text{A.11})$$

where the condition of strict hyperbolicity (5.8) was used. In the heterogeneous case, the elasticities which give the maximum  $R$  should be chosen.

## APPENDIX B

*Free-space Green's function along the symmetry axis for the transversely isotropic solid*

The two-dimensional anisotropic Green's function  $u_{kp}(\mathbf{x}, t)$  satisfies the following equation of motion:

$$c_{ijkl} \frac{\partial^2 u_{kp}}{\partial x_i \partial x_j} + f_{ip} = \rho \frac{\partial^2 u_{ip}}{\partial t^2}, \quad i, j, k, l, p = 1, 2, \quad (\text{B.1})$$

where  $f_{ip}$  is the impulsive body force given by

$$f_{ip} = \delta_{ip} \delta(x) \delta(z) \delta(t). \quad (\text{B.2})$$

Defining the dimensionless variable

$$\bar{z} = z/\tau,$$

with

$$\tau = V_s t,$$

where  $V_s$  is given by equation (5.7), the solution to equation (B.1) for class IV transversely isotropic materials along the symmetry axis  $\mathbf{z}$  is (2, p. 78)

$$u_{xx}(z, t) = u_{xx}(z, t) = 0, \quad (\text{B.3})$$

$$u_{xx}(z, t) = \begin{cases} 0, & 0 \leq t \leq t_p, \\ F_1(\bar{z}), & t_p < t < t_s, \\ 0, & t_s \leq t \leq t_1, \\ F_3(\bar{z}), & t > t_1, \end{cases} \quad (\text{B.4})$$

with

$$F_1(\bar{z}) = \frac{1}{\pi\tau} \left[ \frac{1}{4\beta} - \frac{2\beta(\alpha - \bar{z}^2) - \{\gamma - (\beta + 1)\bar{z}^2\}}{4\beta D^{\frac{1}{2}}} \right] \left[ \frac{-\{\gamma - (\beta + 1)\bar{z}^2\} + D^{\frac{1}{2}}}{-2(\alpha - \bar{z}^2)(1 - \bar{z}^2)} \right]^{\frac{1}{2}},$$

$$F_3(\bar{z}) = \frac{1}{2\pi\tau} \left[ \frac{1}{\beta^{\frac{1}{2}}} + \left( \frac{\alpha - \bar{z}^2}{1 - \bar{z}^2} \right)^{\frac{1}{2}} \right] [\{\gamma - (\beta + 1)\bar{z}^2\} + 2\{\beta(\alpha - \bar{z}^2)(1 - \bar{z}^2)\}^{\frac{1}{2}}]^{-\frac{1}{2}},$$

and

$$u_{zz}(z, t) = \begin{cases} 0, & 0 \leq t \leq t_p, \\ G_1(\bar{z}), & t_p < t < t_s, \\ 0, & t_s \leq t \leq t_1, \\ G_3(\bar{z}), & t > t_1, \end{cases} \quad (\text{B.5})$$

with

$$G_1(\bar{z}) = \frac{1}{\pi\tau} \left[ \frac{1}{4} - \frac{2(1 - \bar{z}^2) - \{\gamma - (\beta + 1)\bar{z}^2\}}{4D^{\frac{1}{2}}} \right] \left[ \frac{-\{\gamma - (\beta + 1)\bar{z}^2\} + D^{\frac{1}{2}}}{-2(\alpha - \bar{z}^2)(1 - \bar{z}^2)} \right]^{\frac{1}{2}},$$

$$G_3(\bar{z}) = \frac{1}{2\pi\tau} \left[ \frac{1}{\beta^{\frac{1}{2}}} + \left( \frac{1 - \bar{z}^2}{\alpha - \bar{z}^2} \right)^{\frac{1}{2}} \right] [\{\gamma - (\beta + 1)\bar{z}^2\} + 2\{\beta(\alpha - \bar{z}^2)(1 - \bar{z}^2)\}^{\frac{1}{2}}]^{-\frac{1}{2}},$$

where

$$t_s = z/(c_{44}/\rho)^{\frac{1}{2}}, \quad t_p = z/(c_{33}/\rho)^{\frac{1}{2}}, \quad t_1 = t_s/\bar{z}_1. \quad (\text{B.6})$$

The quantity  $D(\bar{z})$  is given by

$$D(\bar{z}) = \{\gamma - (\beta + 1)\bar{z}^2\}^2 - 4\beta(\alpha - \bar{z}^2)(1 - \bar{z}^2)$$

and

$$\bar{z}_1 = [\gamma(\beta + 1) - 2\beta(\alpha + 1) + 2\{\beta(1 + \alpha\beta - \gamma)(\alpha + \beta - \gamma)\}^{\frac{1}{2}}]^{1/2}/(\beta - 1). \quad (\text{B.7})$$

To perform the comparison with the numerical solution we convolve the free-space Green's function with the shifted zero-phase pulse function given by (6.1).